Suppression of arsenopyrite oxidation by microencapsulation using ferric-catecholate complexes and phosphate

Ilhwan Park[a,*], Kazuki Higuchi[b], Carlito Baltazar Tabelin[c], Sanghee Jeon[a], Mayumi Ito[a], Naoki Hiroyoshi[a]

[a] Division of Sustainable Resources Engineering, Faculty of Engineering, Hokkaido University, Sapporo, 060-8628, Japan

[b] Division of Sustainable Resources Engineering, Graduate School of Engineering, Hokkaido University, Sapporo, 060-8628, Japan

[c] School of Minerals and Energy Resources Engineering, The University of New South Wales, Sydney, NSW 2052, Australia

Abstract

Mineral processing, pyro- and hydrometallurgical processes of auriferous sulfide ores and porphyry copper deposits (PCDs) generate arsenopyrite-rich wastes. These wastes are disposed of into the tailings storage facilities (TSF) in which toxic arsenic (As) is leached out and acid mine drainage (AMD) is generated due to the oxidation of arsenopyrite (FeAsS). To suppress arsenopyrite oxidation, this study investigated the passivation of arsenopyrite by forming ferric phosphate ($FePO_4$) coating on its surface using ferric-catecholate complexes and phosphate simultaneously. Ferric iron (Fe^{3+}) and catechol form three types of complexes (mono-, bis-, and tris-catecholate complexes) depending on the pH, but mono-catecholate complex (i.e., $[Fe(cat)]^+$) became unstable in the presence of phosphate because the chemical affinity of Fe^{3+}—PO_4^{3-} is most probably stronger than that of Fe^{3+}—catechol in $[Fe(cat)]^+$. When two or more catechol molecules were coordinated with Fe^{3+} (i.e., $[Fe(cat)_2]^-$ and $[Fe(cat)_3]^{3-}$), however, these complexes were stable irrespective of the presence of phosphate. The treatment of arsenopyrite with $[Fe(cat)_2]^-$ and phosphate could suppress its oxidation due to the formation of $FePO_4$ coating, evidenced by SEM-EDX and XPS analyses. The mechanism of $FePO_4$ coating formation by $[Fe(cat)_2]^-$ and phosphate was confirmed by linear sweep voltammetry (LSV): (1) $[Fe(cat)_2]^-$ was oxidatively decomposed and

(2) the resultant product (i.e., $[Fe(cat)]^{+}$) reacts with phosphate, resulting in the formation of $FePO_4$.

Keywords: arsenopyrite, passivation, ferric-catecholate complexes, phosphate, ferric phosphate coating

1. Introduction

Arsenopyrite (FeAsS), the most common arsenic (As)-bearing sulfide mineral in nature, is often found in auriferous sulfide ores. Due to the fact that arsenopyrite is one of the most common hosts of invisible gold (Au), which is optically undetectable Au particles because of its incorporation into the structure of host minerals, auriferous sulfide ores are typically processed by flotation to recover the bulk of gold-bearing arsenopyrite, and then flotation concentrates are processed via pretreatment (e.g., acidic pressure oxidation (Gudyanga et al., 1999), alkaline pretreatment (Espitia and Lapidus, 2015), biooxidation (Ciftci and Akcil, 2010), pyrolysis (Dunn and Chamberlain, 1997), ultra-fine grinding (Corrans and Angove, 1991)) to expose Au particles encapsulated in host minerals followed by cyanidation—a conventional hydrometallurgical technique for the selective leaching of gold (Asamoaha et al., 2018; Deol et al., 2012; Pokrovski et al., 2019; Tabelin et al., 2020a). Because arsenopyrite is not dissolved during cyanidation, it ends up with the leaching residues typically disposed of into tailings storage facilities (TSF). In addition, arsenopyrite is also found in porphyry copper deposits (PCDs)—the world's most important source of copper (Cu) accounting for more than 60% of the annual world copper production (John et al., 2010; John and Taylor, 2016). Michiquillay (Peru), Potrerillos (Chile), and Río Blanco-Los Bronces (Chile) are the examples of PCDs containing arsenopyrite (Berger et al., 2008). In the flotation of PCDs, however, the recovery of arsenopyrite is unfavorable because Cu concentrates with high contents of As are highly penalized by smelters. Because of strict emission standards for As, smelters in recent years will only treat Cu concentrates with < 0.5% As, and penalties of around US$3 per 0.1 wt% is charged above 0.2 wt% As (Bruckard et al., 2010; Lane et al., 2016; Nazari et al., 2017). Because of this, almost all arsenopyrite is removed during bulk flotation of PCDs, and the generated As-rich tailings are discarded.

When arsenopyrite is exposed to oxygen and water, it is readily oxidized and releases toxic As into the surrounding environment (Eqs. (1)–(3)).

$$4FeAsS_{(s)} + 11O_{2(aq)} + 6H_2O \rightarrow 4Fe^{2+}{}_{(aq)} + 4H_3AsO_{3(aq)} + 4SO_4{}^{2-}{}_{(aq)} \quad (1)$$

$$4Fe^{2+}_{(aq)} + O_{2(aq)} + 4H^{+}_{(aq)} \rightarrow 4Fe^{3+}_{(aq)} + 2H_2O \quad (2)$$

$$FeAsS_{(s)} + 13Fe^{3+}_{(aq)} + 8H_2O \rightarrow 14Fe^{2+}_{(aq)} + H_3AsO_{4(aq)} + SO_4{}^{2-}_{(aq)} + 13H^{+}_{(aq)} \quad (3)$$

Arsenic and its compounds are strictly regulated substances because they have been reported to cause numerous diseases like hyperpigmentation, keratosis, anemia, and neuropathy (Mohan and Pittman, 2007; Tabelin et al., 2017a, 2017b). When ingested continuously for prolonged periods of time via contaminated drinking water, for example, the risk of developing several types of cancers is greatly increased (Boddu et al., 2008; Huyen et al., 2019a, 2019b; Tabelin et al., 2018, 2020b). Because of this, the maximum contaminant level (MCL) for As in drinking water has been set at 10 μg/L (USEPA, 2001). Aside from being a substantial source of As, arsenopyrite also has an acidification potential (AP) about three times higher than pyrite, which means that its oxidation together with that of pyrite is the primary cause of acid mine drainage (AMD) formation (Chopard et al., 2017; Park et al., 2019; Tabelin et al., 2017c, 2017d). AMD is the acidic leachate (pH < 3) generated in old TSFs, abandoned underground mine sites and pyrite-bearing waste rock dumps polluted with heavy metals and toxic metalloids (Igarashi et al., 2020; Tabelin et al., 2009, 2013; Tatsuhara et al., 2012; Tomiyama et al., 2019, 2020).

Arsenopyrite dissolves electrochemically in the presence of oxidants and water, so the suppression of their interactions with mineral is a key point for limiting the release of As and AMD formation resulting from arsenopyrite oxidation. One promising approach is the direct passivation of this problematic mineral via microencapsulation. Evangelou (1995) introduced a microencapsulation technique using hydrogen peroxide (H_2O_2) and dipotassium hydrogen phosphate (K_2HPO_4) to passivate pyrite with ferric phosphate ($FePO_4$) coating. In this technique, pyrite passivation was achieved via the following steps: (1) H_2O_2 oxidizes pyrite and generates Fe^{3+} near the pyrite surface, and (2) Fe^{3+} reacts with phosphate and precipitates as $FePO_4$ on the pyrite surface. Although effective, there are some serious drawbacks of this technique; for example, (1) the use of H_2O_2 to pre-oxidize sulfide minerals and generate Fe^{3+} is problematic because handling and storage of this compound, especially in large quantities, are very challenging (Barreiro et al., 2007; Ouyang et al., 2015), (2) the technique cannot target sulfide minerals in complex wastes like tailings, which typically contain < 10% sulfide minerals (Blowes et al., 1998), resulting in unwanted large consumption of this expensive reagents, and (3) high concentration of As is most likely leached out during treatment due to the strong oxidizing ability of H_2O_2.

To overcome the limitations of using H_2O_2, many alternative techniques have been recently developed: (1)

formation of organic coatings using sodium oleate (Jiang et al., 2000), humic acid (Ačai et al., 2009), phospholipids (Elsetinow et al., 2003), (2) formation of silane-based coatings using alkoxysilanes (Dong et al., 2020; Liu et al., 2017), and (3) carrier-microencapsulation (CME) using metal-organic complexes (e.g., $[Ti(cat)_3]^{2-}$, $[Al(cat)_n]^{3-2n}$, $[Fe(cat)_n]^{3-2n}$; where "cat" is catechol (1,2-dihydroxybenzene, $C_6H_4(OH)_2$) and "n" is the number of catechol molecules in the range of 1–3) (Li et al., 2019; Park et al., 2018a, 2018b, 2020a). All these techniques are effective in suppressing arsenopyrite/pyrite oxidations, but each of them has apparent drawbacks. For example, organic coatings would be stable for a relatively short period of time because in nature, there are various types of microorganisms that can degrade even very complex organic compounds. Meanwhile, silane-based coatings have a better durability than that of organic coatings, but the lack of ability of alkoxysilanes to selectively target the problematic minerals like arsenopyrite and pyrite would be one of the problems in its application to real mine wastes. In the case of CME, inorganic coatings (e.g., metal-oxyhydroxides) could be selectively formed on the surfaces of arsenopyrite and pyrite; however, the stability of metal-oxyhydroxide coatings is lower than that of $FePO_4$ coating under strongly acidic conditions (< pH 3). Thus, an improved microencapsulation technique having abilities to not only target arsenopyrite as well as other problematic minerals but also create stable coatings is required to be developed.

The above-mentioned limitations of Evangelou's technique forming $FePO_4$ coating using K_2HPO_4 and H_2O_2 could be addressed by adopting alternative ways of supplying Fe^{3+} to facilitate microencapsulation of sulfide minerals. For example, in CME, a technique that forms a surface protective coating on the surface of sulfide minerals like arsenopyrite and pyrite, metal-organic complexes are used to deliver metal ions to the arsenopyrite/pyrite surfaces (Li et al., 2019; Park et al., 2018a, 2018b, 2020a). Metal ion is released from the complex via its oxidative decomposition taking place only on the surface of semi-conducting minerals. Therefore, the use of Fe^{III}-catecholate complexes can be a promising alternative to the use of H_2O_2 because of its ability to selectively supply Fe^{3+} to the surface of arsenopyrite. In this study, a new passivation approach via simultaneous use of Fe-catecholate complexes and phosphate to create $FePO_4$ coating on arsenopyrite was investigated. Specifically, the objectives of this study are as follows: (1) to evaluate the stability and oxidative decomposition behavior of Fe-catecholate complexes without and with phosphate by linear sweep voltammetry (LSV), (2) to elucidate the passivation of arsenopyrite using leaching tests under various conditions, and (3) to determine important suppression or passivation mechanisms using surface-sensitive characterization techniques like scanning electron microscopy with energy dispersive X-ray spectroscopy (SEM-EDX) and X-ray photoelectron

spectroscopy (XPS).

2. Materials and methods

2.1. Arsenopyrite sample

The arsenopyrite sample used in this study was obtained from Toroku mine, Miyazaki, Japan. It was crushed by a jaw crusher (BB 51, Retsch Inc., Germany), ground in a vibratory disc mill (RS 100, Retsch Inc., Germany), and then screened to obtain a size fraction of 100–150 μm. This sample is mainly composed of arsenopyrite (67%) with pyrite (13%) and quartz (15%) as minor mineral impurities (Park et al., 2018a). Details of sample characterizations are provided as supplementary information (Fig. S1 and Tables S1). Prior to the leaching experiments, the sample (100–150 μm) was washed to remove slime coating and any oxidized layer formed during preparation and storage by the method of McKibben et al. (2008): (i) ultrasonic desliming in methanol, (ii) washing with 1.8 M HNO_3, (iii) rinsing with deionized (DI) water, (iv) dewatering with acetone, and (v) drying in a vacuum desiccator.

2.2. Stability of Fe-catecholate complexes in the absence and presence of phosphate

For passivation of arsenopyrite to be selective, the complex should be oxidatively decomposed only on the mineral's surface and not in the bulk solution. To evaluate the stability of Fe-catecholate complexes in a system containing phosphate, solutions containing 1 mM $FeCl_3 \cdot 6H_2O$ with (i) none, (ii) 1 mM NaH_2PO_4, (iii) 3 mM pyrocatechol, and (iv) 3 mM pyrocatechol and 1 mM NaH_2PO_4 were prepared, and its pH was adjusted from 2 to 11 using 0.1 and 1.0 M HCl and NaOH. All chemicals used in this study were of reagent grade (Wako Pure Chemical Industries, Ltd., Japan). Once the solution pH reached predetermined values, it was allowed to stabilize for 10 min. Afterward, the solutions were filtered through 0.2 μm syringe-driven membrane filters (LMS Co. Ltd., Japan) to remove precipitates and polymerized organic molecules, and the filtrates were analyzed by an inductively coupled plasma atomic emission spectrometer (ICP-AES, ICPE-9820, Shimadzu Corporation, Japan) to measure the concentration of dissolved Fe. Similarly, control experiments were conducted using solutions consisting of 1 mM Fe^{3+} with and without 1 mM NaH_2PO_4 to check the solubility of each precipitate as a function of pH. The precipitates formed during the experiments were collected and analyzed by attenuated total reflectance

Fourier transform infrared (ATR–FTIR) spectroscopy (FT/IR-6200 HFV and ATR Pro One attachment equipped with a diamond prism, Jasco Analytical Instruments, Japan) under the following conditions: 1000 scans at a resolution of 4 cm^{-1} and in the range of 400–4000 cm^{-1}. As a reference, iron(III) phosphate n-hydrate ($FePO_4 \cdot nH_2O$) (Wako Pure Chemical Industries, Ltd., Japan) was also analyzed by ATR-FTIR.

2.3. Oxidative decomposition of Fe-catecholate complexes in the absence and presence of phosphate

Oxidative decomposition of bis-catecholate complex (i.e., $[Fe(cat)_2]^-$) in the presence of phosphate was investigated by linear sweep voltammetry (LSV). For this, an electrochemical measurement unit (SI 1280B, Solartron Instruments, UK) with a conventional three-electrode system consisting of a platinum (Pt) electrode, a Pt wire, and an Ag/AgCl electrode (filled with 3.3 M NaCl solution) was used as working, counter, and reference electrodes, respectively. The LSV measurement was conducted in the solution containing 1 mM $FeCl_2 \cdot 6H_2O$, 2 mM pyrocatechol (denoted as H_2cat), and 1 mM NaH_2PO_4, the pH of which was adjusted to 7 where bis-catecholate complex is dominant. Prior to LSV measurement, the solution was filtered through a 0.2 μm syringe-driven membrane filter, deoxygenated by N_2 purging, and equilibrated at 25°C for 30 min. Afterward, the working electrode was equilibrated at open circuit potential (OCP) and then anodically polarized up to +1.0 V vs. SHE at a scan rate of 5 mV/s. For the comparison, LSV measurements of mono-catecholate complex ($[Fe^{3+}]$, 1 mM; $[H_2cat]$, 1 mM; pH, 5), bis-catecholate complex (($[Fe^{3+}]$, 1 mM; $[H_2cat]$, 2 mM; pH, 7), and catechol ($[H_2cat]$, 2 mM; pH, 7) were also conducted via an identical procedure as mentioned above. All solutions contain 0.1 M NaCl (Wako Pure Chemical Industries, Ltd., Japan) as a supporting electrolyte.

2.4. Passivation of arsenopyrite by microencapsulation using Fe-catecholate complex with and without phosphate

To check the passivation of arsenopyrite by microencapsulation using Fe-catecholate complex with and without phosphate, three types of solutions (e.g., DI water (control), 5 mM $[Fe(cat)_2]^-$ only, and 5 mM $[Fe(cat)_2]^-$ with 5 mM PO_4^{3-}), all of which were adjusted to pH 7, were prepared. One gram of washed arsenopyrite was mixed with 10 mL of prepared solution in a 50-mL Erlenmeyer flask and shaken at 120 min^{-1} in a constant temperature water bath shaker (25 °C) for 3 days. At predetermined time intervals, samples were filtered through

0.2 μm syringe-driven membrane filters, and the filtrates were analyzed by ICP-AES. Some experiments were done in triplicates. Meanwhile, the residues were thoroughly washed with DI water, dried in a vacuum oven at 40°C for 24 h, and analyzed by SEM-EDX (JSM-IT200, JEOL Ltd., Japan) and XPS (JPS-9200, JEOL Ltd., Japan). The XPS analysis was conducted using a monochromatized Al Kα X-ray source (1486.7 eV) operated at 300 W (Voltage, 12 kV; Current, 25 mA) with charge neutralization under ultrahigh vacuum conditions (approximately 10^{-7} Pa). Narrow scan spectra of Fe $2p_{3/2}$, As $3d_{5/2}$, S $2p_{3/2}$, and P $2p_{3/2}$ were obtained and calibrated using the binding energy of adventitious carbon (C 1s) (285.0 eV) for charge correction. For deconvolutions of the spectra, XPSPEAK version 4.1 was used with an 80% Gaussian–20% Lorentzian peak model and a true Shirley background (Nesbitt and Muir, 1994; Shirley, 1972).

2.5. Leachability tests of treated-arsenopyrite

After 3-day treatments of arsenopyrite by control, Fe-catecholate complex with and without phosphate, the stability of coating and leachabilities of Fe and As from treated samples were investigated. For this, one gram of treated arsenopyrite and 10 mL of DI water were put in a 50-mL Erlenmeyer flask and shaken at 120 min^{-1} and 25 °C for 24 h. After this, the suspension pH was measured, and the filtrates collected after filtration using 0.2 μm syringe-driven membrane filters were analyzed by ICP-AES to measure the concentrations of Fe and As released from untreated and treated samples. All tests were done in triplicates.

2.6. Chronoamperometry measurements

Chronoamperometry was adopted to evaluate the anodic half-cell reactions of untreated arsenopyrite and the one treated with $[Fe(cat)_2]^-$ and phosphate. For this, a mineral working electrode was prepared as follows: (i) arsenopyrite sample was cut using a diamond cutter, (ii) connected to a copper wire with silver conducting paste (DOTITE, Fujikura Kasei Co., Ltd., Japan), and (iii) fixed inside a plastic holder with Technovit® non-conductive resin (Heraeus Kulzer GmbH, Germany). Afterward, the prepared mineral electrode was polished using a polishing machine (SAPHIR 250 M1, ATM GmbH, Germany) with a series of silicon carbide papers (P320, P600, and P1200) and diamond suspensions (3 and 1 μm) to expose a new and unreacted surface. Two-set of experiments were conducted using untreated mineral electrode and the one treated with 5 mM $[Fe(cat)_2]^-$ with 5

mM PO_4^{3-} for 3 days. Untreated or treated mineral working electrode, Pt counter electrode, and Ag/AgCl (filled with saturated KCl) reference electrode were immersed into the electrolyte solution (0.1 M Na_2SO_4) and connected to potentiostat/galvanostat (SP-300, BioLogic, France). After measuring OCP under N_2 atmosphere, a fixed potential of 0.7 V vs. SHE was applied to the working electrode for 1 h with magnetic stirring at 250 rpm. This applied potential was chosen based on typical redox conditions where AMD has been formed (i.e., about 0.64–0.68 V) (Yamaguchi et al., 2015).

3. Results and discussion

3.1. Stability of Fe-catecholate complexes in the absence and presence of phosphate

Catechol is known to form three types of complexes with Fe^{3+} depending on the pH; that is, mono-catecholate ($[Fe(cat)]^+$), bis-catecholate ($[Fe(cat)_2]^-$), and tris-catecholate ($Fe(cat)_3]^{3-}$) complexes are dominant at pH 3.0–5.5, 5.5–9.0, and >9.0, respectively (Li et al., 2019). The formation of Fe-catecholate complexes was also experimentally confirmed in this study. In the absence of any chelators, Fe^{3+} starts precipitating at above pH 3, most of which are precipitated when pH is greater than 4. However, the addition of catechol dramatically changes the solubility of Fe^{3+} (Fig. 1a). From pH 3 to 5, dissolved Fe concentration decreased from about 1.0 to 0.8 mM, then it increased as the pH increased above 5.0. This change in the solubility of Fe^{3+} could be achieved due to the formation of three types of Fe-catecholate complexes (i.e., $[Fe(cat)]^+$, $[Fe(cat)_2]^-$, and $Fe(cat)_3]^{3-}$). When phosphate is present in the Fe-catechol system, dissolved Fe concentration was considerably changed in the pH range of 4.0–6.0; that is, dissolved Fe concentration was lower compared to that without phosphate. In this pH range, the dominant species of Fe-catecholate complex is $[Fe(cat)]^+$, which became unstable in the presence of phosphate. This implies that the chemical affinity of Fe^{3+}—catechol in $[Fe(cat)]^+$ is weaker than that of Fe^{3+}—phosphate, and thereby catechol molecule coordinated with Fe^{3+} is replaced with phosphate as illustrated in the following equation:

$$[Fe(cat)]^+ + H_2PO_4^- \rightarrow FePO_4\downarrow + H_2cat \quad (4)$$

This deduction on the formation of $FePO_4$ is supported by ATR-FTIR analysis of the precipitate formed in solution containing $[Fe(cat)]^+$ and phosphate at pH 5 (Fig. 1b). As shown in the FTIR spectrum of precipitate, the absorption bands detected in 3500–3000 and 1700–1600 cm^{-1} regions are the stretching and bending vibrations of water molecules, respectively (Boonchom and Puttawong, 2010; Zaghib and Julien, 2005). The symmetric (ν_1)

and antisymmetric stretching (ν_3) modes of the P–O bonds are observed in 1200–900 cm^{-1} region (Fig. 1b) while IR absorption bands observed at 610, 583, and 542 cm^{-1} are attributed to antisymmetric bending mode (ν_4) of O–P–O (Fig. 1b-1) (Boonchom and Puttawong, 2010; Zaghib and Julien, 2005). These IR signatures of precipitate are almost the same as that of $FePO_4$ reagent (Fig. 1b-2), indicating that the precipitate formed between $[Fe(cat)]^+$ and phosphate is most likely $FePO_4$ as illustrated in Eq. (4).

The stability of complex(es) is of importance because it is directly related to its selectivity for acid-generating minerals like sulfide minerals in a complex system (e.g., TSF in which sulfide contents are < 10%; Blowes et al., 1998). For the selective passivation of sulfide minerals by Fe-catecholate complexes and phosphate, the former should be oxidatively decomposed only on the mineral surface, not precipitated in the bulk solution. Based on this, pH >7.0 at which Fe-catecholate complexes (e.g., $[Fe(cat)_2]^-$ and $[Fe(cat)_3]^{3-}$) are stable in the presence of phosphate could be considered as suitable conditions for selective passivation of arsenopyrite; however, in this study, all the experiments were conducted at pH 7.0 to synthesize $[Fe(cat)_2]^-$ because the oxidative decomposition of $[Fe(cat)_3]^{3-}$ was reported to be sluggish compared to $[Fe(cat)_2]^-$ (Li et al., 2019).

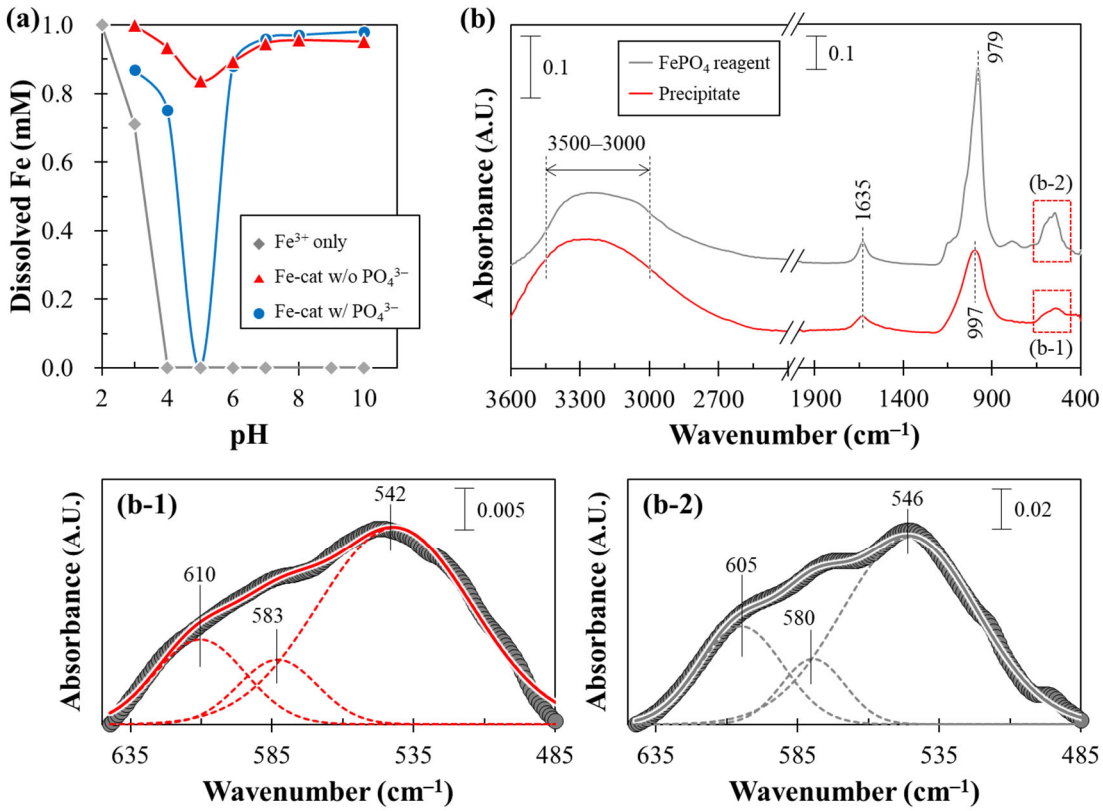

Fig. 1. (a) Solubility of Fe with pH in Fe only, Fe-catechol and Fe-catechol-phosphate systems ($[Fe^{3+}]$ = 1 mM,

233 [H_2cat] = 3 mM, [PO_4^{3-}] = 1 mM), (b) ATR-FTIR spectra of $FePO_4$ reagent and the precipitate formed in solution
234 containing Fe^{3+}, H_2cat , and PO_4^{3-} at pH 5, and deconvoluted spectra between 645 and 485 cm^{-1} of the precipitate
235 (b-1) and $FePO_4$ reagent (b-2).

236

237 *3.2. Effects of phosphate on the oxidative decomposition of Fe-catecholate complexes*

238 Linear sweep voltammetry (LSV) was conducted to understand the mechanisms of how Fe-catecholate
239 complexes are oxidatively decomposed in the absence and presence of phosphate (Fig. 2). As shown in LSV of
240 Fe-catechol system at pH 7, there are two apparent anodic peaks observed at around 0.49 V (A_1) and 0.64 V (A_2).
241 The dominant species of Fe-catecholate complex at pH 7 is $[Fe(cat)_2]^-$, so the first anodic peak (A_1) could be
242 considered as its oxidative decomposition to $[Fe(cat)]^+$ as shown in the following reaction:

243 $$[Fe(cat)_2]^- \rightarrow [Fe(cat)]^+ + Q + 2e^- \quad (5)$$

244 where Q denotes ortho-quinone (1,2-benzoquinone, $C_6H_4O_2$), the oxidation product of catechol. Meanwhile, the
245 second anodic peak (A_2) appeared, which indicates that $[Fe(cat)]^+$ is further oxidized, resulting in the release of
246 Fe^{3+} as the applied potential increases (Eq. (6)). The LSV of Fe-catechol system at pH 5 where $[Fe(cat)]^+$ is
247 dominant also supports that the anodic peak at 0.64 V (A_2) could be related to the oxidative decomposition of
248 $[Fe(cat)]^+$.

249 $$[Fe(cat)]^+ \rightarrow Fe^{3+} + Q + 2e^- \quad (6)$$

250 In the presence of phosphate, two anodic peaks were also observed in the LSV of $[Fe(cat)_2]^-$. The first peak
251 (A_1) appeared at almost the same potential as that for the decomposition of $[Fe(cat)_2]^-$ to $[Fe(cat)]^+$ observed in
252 LSV of $[Fe(cat)_2]^-$ only. The succeeding peak (A_3), however, was shifted from 0.64 to 0.70 V when phosphate was
253 present, which indicates that this anodic peak does not probably arise from the oxidative decomposition of
254 $[Fe(cat)]^+$. The LSV of catechol only solution at pH 7 showed that an anodic peak appeared at almost the same
255 position as the second anodic peak observed in LSV of $[Fe(cat)_2]^-$ with phosphate, indicating that this anodic peak
256 (A_3) most likely resulted from the oxidation of free catechol molecules. As discussed above (section 3.1), when
257 $[Fe(cat)]^+$ and phosphate react, $FePO_4$ and free catechol are produced (Eq. (4)), which supports A_3 peak
258 corresponds to the anodic reaction of catechol. From these results, the mechanism of the complex decomposition
259 process in the presence of phosphate could be elucidated as follows: (i) $[Fe(cat)_2]^-$ is oxidatively decomposed (Eq.

(5)) and (ii) its resultant product (i.e., $[Fe(cat)]^{+}$) reacts with phosphate, followed by the formation of $FePO_4$ and free catechol (Eq. (4)).

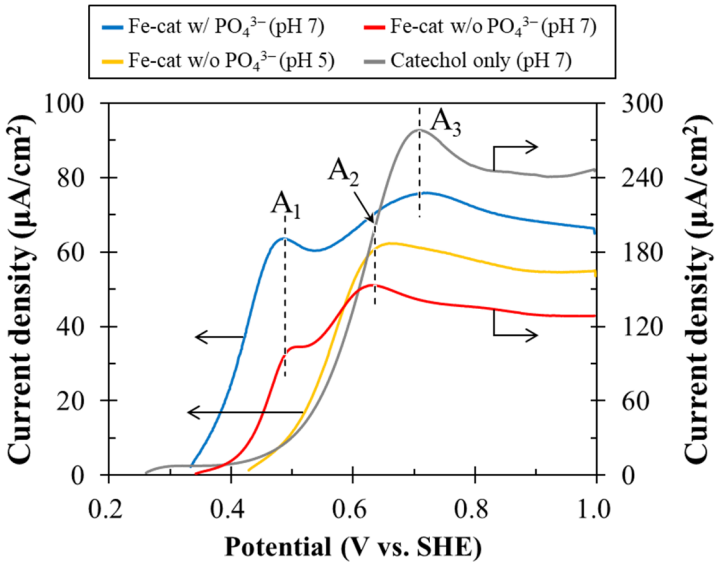

Fig. 2. Linear sweep voltammograms of catechol only at pH 7 ($[H_2cat]$ = 1 mM), Fe-catechol only at pH 5 and 7 ($[Fe^{3+}]$ = 1 mM, $[H_2cat]$ = 1 mM (pH 5) and 2 mM (pH 7)), and Fe-catechol-phosphate at pH 7 ($[Fe^{3+}]$ = 1 mM, $[H_2cat]$ = 2 mM, $[PO_4^{3-}]$ = 1 mM). Note that two different scales for current density are used and indicated by arrows.

3.3. Passivation of arsenopyrite by microencapsulation using Fe-catecholate complex with and without phosphate

In the control experiment, the leachate pH was continuously decreased from 7.0 to 2.7 while the other two cases were kept almost constant due to the buffering effects of Fe-catecholate complexes and phosphate (Fig. 3a). Arsenopyrite was oxidized rapidly in the control; that is, dissolved As and Fe concentrations after 3 days reached around 2.0 and 1.3 mM, respectively (Figs. 3b and 3c). Compared to this, when arsenopyrite was treated in the solution containing Fe-catecholate complex, the release of As from arsenopyrite was apparently suppressed; that is, dissolved As concentration after 3 days was around 0.7 mM—the released amount of As decreased by 65% compared to that of control (Fig. 3b). It is also interesting to note that dissolved Fe concentration kept decreasing with time (Fig. 3c), which indicates that $[Fe(cat)_2]^{-}$ was sequentially decomposed (Eqs. (5) and (6)), then Fe^{3+} released from the complex was precipitated (Eq. (7)).

278 $Fe^{3+} + 3H_2O \leftrightarrow Fe(OH)_3\downarrow + 3H^+$ (7)

279 In our previous study on microencapsulation of pyrite using Fe-catecholate complexes, it was confirmed that
280 $[Fe(cat)]^+$ and $[Fe(cat)_2]^-$ formed the surface protective coating composed of Fe-oxyhydroxide on pyrite (Li et al.,
281 2019), so arsenopyrite could also be passivated via the identical way, thereby suppressing the release of As from
282 arsenopyrite. In the presence of phosphate, however, the behaviors of As release as well as Fe precipitation
283 changed significantly: (i) dissolved As concentration was rapidly increased to 0.7 mM for 1 day similar to that of
284 control, but did not increase further, and (ii) dissolved Fe concentration increased from 3.8 to 4.1 mM after 1 day,
285 then decreased to 3.7 mM after 3 days (Figs. 3b and 3c). Based on the relationship between the released amounts
286 of As and Fe measured in the control experiment, the released amounts of Fe including both dissolved and
287 precipitated species were roughly estimated (see the dotted lines in Fig. 3c). As it can be seen, the precipitation of
288 dissolved Fe was negligible during 1-day leaching in the presence of phosphate but after 3 days, around 0.6 mM
289 of dissolved Fe was precipitated. This is substantially lower compared to the result in the absence of phosphate
290 (i.e., Fe-catecholate complex only) that around 1.8 mM of dissolved Fe was precipitated. These changes in As
291 release and Fe precipitation are most likely caused by the presence of phosphate that adsorbed to the surface of
292 arsenopyrite. As shown in Fig. 3d, dissolved P concentration decreased by 15% for 1 day even though dissolved
293 Fe was not nearly precipitated. This implies that the decrease in dissolved P concentration was mainly attributed
294 to its adsorption on the surface of arsenopyrite, not the precipitation with Fe^{3+} forming $FePO_4$ (Eq. (4)). This
295 deduction is supported by phosphate sorption test which revealed that when arsenopyrite reacted with phosphate
296 only for 1 day, dissolved P was adsorbed on arsenopyrite surface, so its concentration decreased to a similar level
297 as for Fe-catecholate complex with phosphate (Fig. 3d). Elsetinow et al. (2001) reported that phosphate is adsorbed
298 on pyrite surface, then adsorbed phosphate may act as a site blocker for molecular oxygen adsorption and/or alter
299 the electronic structure of the Fe(III)-oxyhydroxide phases, which make electron transfer less energetically
300 favorable. Similarly, adsorbed phosphate could also limit the electrochemical reaction of arsenopyrite, and thus
301 the decomposition of Fe-catecholate complexes becomes sluggish compared to that in the absence of phosphate.
302 On the other hand, after 3 days, both dissolved Fe and P concentrations decreased (Figs. 3c and 3d). It is
303 noteworthy that dissolved P concentration obtained in the sorption test was almost not changed from 1 to 3 days,
304 indicating that the decreases in Fe and P concentrations are most likely caused by their precipitation. The decreased
305 Fe and P concentrations were both around 0.6 mM, implying that the precipitate with 1:1 stoichiometric ratio of
306 Fe^{3+}:PO_4^{3-} (i.e., $FePO_4$) was formed. Assuming that (i) the shape of arsenopyrite is sphere, (ii) all the precipitates

307 are present on arsenopyrite, and (iii) Fe^{3+} and PO_4^{3-} are precipitated as $FePO_4$, the thickness of coating was
308 theoretically calculated to be around 38 nm (see Supplementary Information).

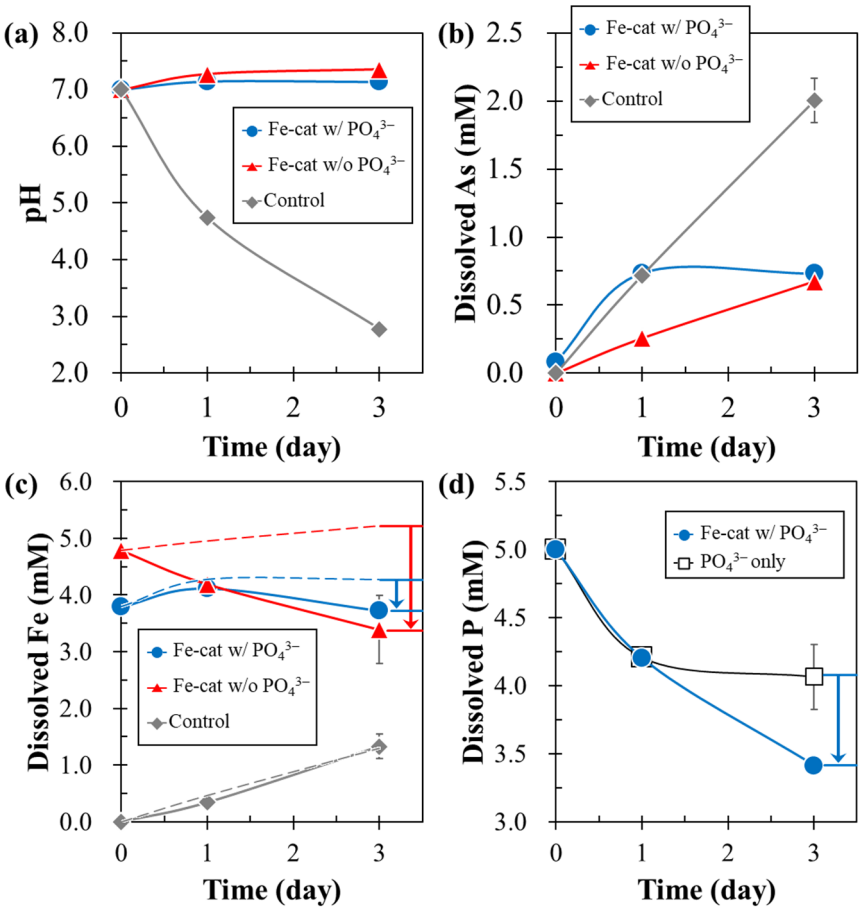

309

310 Fig. 3. Effects of Fe-catecholate complex and phosphate on arsenopyrite oxidation: changes in (a) pH, (b)
311 dissolved As, (c) dissolved Fe (measured), and (d) dissolved P. Note that dotted lines in Fig. 3c denote total Fe
312 concentrations including soluble and precipitated Fe species calculated based on the stoichiometry on the basis of
313 dissolved As concentration measured in the control experiment ($[Fe]_{tot} = 1.3/2.0\ [As]_{dissolved}$).

314

315 The residue treated with Fe-catecholate complex and phosphate for 3 days was analyzed by SEM-EDX, and
316 it shows that on the surface of arsenopyrite, the signal of P was detected (Fig. S2). The weak signal of P indicates
317 that the thickness of P-containing coating is probably thin, so the strong arsenopyrite signals (i.e., Fe, As, and S)
318 are detected. To examine the coating in more detail, arsenopyrite treated with Fe-catecholate complex and
319 phosphate was analyzed by XPS, which is suitable for analyzing very thin layer of coating (around ~6 nm). The
320 XPS narrow-scan spectra of Fe $2p_{3/2}$, As $3d_{5/2}$, S $2p_{3/2}$, and P $2p_{3/2}$ are illustrated in Fig. 4 and the corresponding

curve fitting parameters are summarized in Table 1. The Fe $2p_{3/2}$ spectrum (Fig. 4a) suggests that the outermost surface of treated arsenopyrite consists of (1) arsenopyrite ($Fe^{(II)}$–(AsS) at 707.6 eV), (2) partly oxidized arsenopyrite ($Fe^{(III)}$–(AsS) at 709.2 eV), (3) ferric-oxyhydroxide ($Fe^{(III)}$–O at 710.7 eV), and (4) ferric sulfate ($Fe^{(III)}$–SO_4 at 714.3 eV) (Corkhill and Vaughan, 2009; Grosvenor et al., 2004; Lara et al., 2016; Liu et al., 2020; Nesbitt et al., 1995; Zhu et al., 2014). These assignments are supported by the As $3d_{5/2}$ and S $2p_{3/2}$ spectra (Figs. 4b and 4c); that is, the deconvoluted peaks of $As^{(-I)}$–S (41.6 eV) and $(AsS)^{2-}$ (162.5 eV) observed in the As $3d_{5/2}$ and S $2p_{3/2}$ spectra, respectively, are identified as originating from arsenopyrite/partly oxidized arsenopyrite while a peak of SO_4^{2-} (167.9 eV) implies the presence of ferric sulfate (Han et al., 2011; Liu et al., 2020; Zhu et al., 2014). Moreover, the appearance of $As^{(II)}$–S (42.8 eV) and $As^{(III)}$–S (43.6 eV) coupled with S_2^{2-} (162.5 eV) and S_n^{2-} ($n > 2$; 163.5 eV) indicates the formation of realgar (As_2S_2) and orpiment (As_2S_3), and the remaining species in the As $3d_{5/2}$ spectrum (i.e., $As^{(III)}$–O (44.7 eV)) arise from the soluble As species like AsO_3^{3-} (Fan et al., 2018; Liu et al., 2020). As illustrated in Fig. 4d-1, the deconvoluted P $2p_{3/2}$ spectrum of arsenopyrite treated with "Fe-catecholate complex and phosphate" show three peaks of adsorbed PO_4^{3-} (132.5, 131.4, and 130.0 eV)—these were also observed in the spectrum of phosphate-adsorbed arsenopyrite (Fig. 4d-2))—and a single peak at 133.4 eV, which is assigned to $P^{(V)}$–O binding energy of ferric phosphate (Praneetha and Murugan, 2013; Wang et al., 2013; Zeng et al., 2017; Zhou et al., 2014). The XPS results revealed that the outermost surface of arsenopyrite treated with Fe-catecholate complex and phosphate is composed of not only its oxidation products (e.g., ferric-oxyhydroxide, ferric sulfate, realgar, orpiment, and soluble As species) but also ferric phosphate. Based on the results of LSV, leaching test, and surface analyses, the mechanism of coating formation by Fe-catecholate complex and phosphate was confirmed: (i) $[Fe(cat)_2]^-$ is oxidatively decomposed to $[Fe(cat)]^+$ on the arsenopyrite surface, (ii) $[Fe(cat)]^+$ reacts with phosphate, and (iii) $FePO_4$ coating is formed on the surface of arsenopyrite.

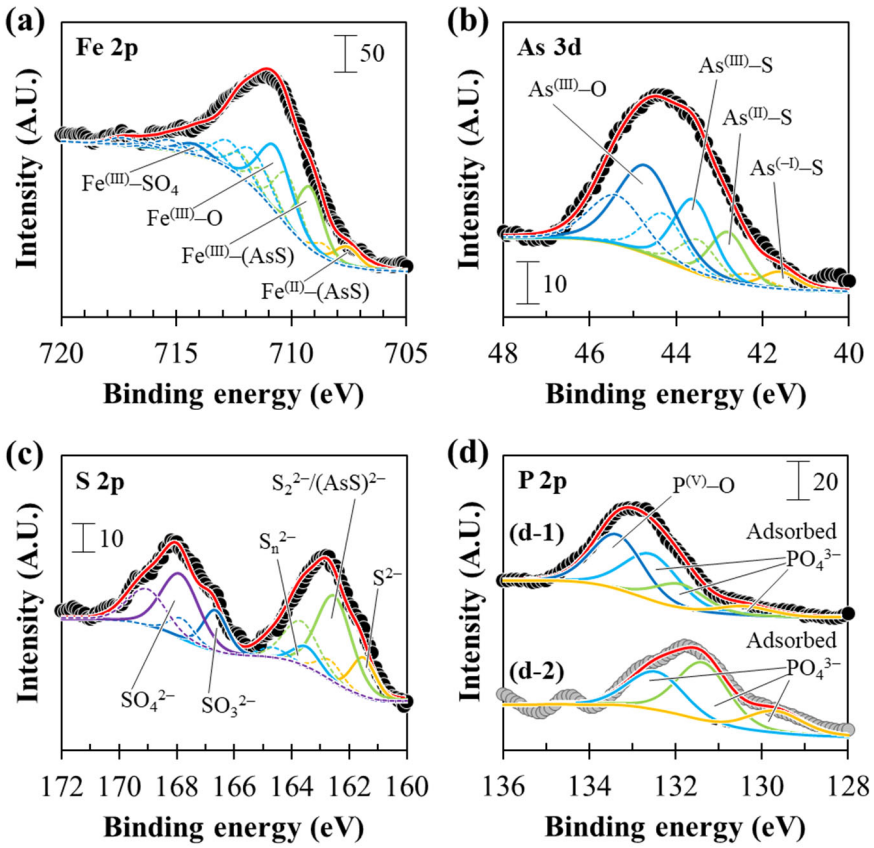

342

343 Fig. 4. XPS spectra of arsenopyrite treated with Fe-catecholate complex and phosphate for 3 days: (a) Fe $2p_{3/2}$, (b)

344 As $3d_{5/2}$, (c) S $2p_{3/2}$, and (d) P $2p_{3/2}$ (d-1: arsenopyrite treated with Fe-catecholate complex and phosphate, d-2:

345 arsenopyrite treated with phosphate only).

346

Table 1. XPS peak parameters and chemical states of Fe, As, S, and P obtained from arsenopyrite treated with Fe-catecholate complex and phosphate for 3 days.

Spectral peak	Binding energy (eV)	FWHM	Chemical states
Fe $2p_{3/2}$[a]	707.6±0.1	1.2	$Fe^{(II)}$–AsS
Fe $2p_{3/2}$[b]	709.2±0.1	1.3	$Fe^{(III)}$–AsS
Fe $2p_{3/2}$[b]	710.7±0.1	1.7	$Fe^{(III)}$–O
Fe $2p_{3/2}$[b]	714.3±0.1	1.5	$Fe^{(III)}$–SO_4
As $3d_{5/2}$[c]	41.6±0.1	1.0	$As^{(-I)}$–S
As $3d_{5/2}$[c]	42.8±0.1	1.0	$As^{(II)}$–S
As $3d_{5/2}$[c]	43.6±0.1	1.1	$As^{(III)}$–S
As $3d_{5/2}$[c]	44.7±0.1	1.5	$As^{(III)}$–O
S $2p_{3/2}$[d]	161.5±0.1	1.0	S^{2-}
S $2p_{3/2}$[d]	162.5±0.1	1.4	S_2^{2-}/$(AsS)^{2-}$
S $2p_{3/2}$[d]	163.5±0.1	1.1	S_n^{2-} (n > 2)
S $2p_{3/2}$[d]	166.7±0.1	1.0	SO_3^{2-}
S $2p_{3/2}$[d]	167.9±0.1	1.5	SO_4^{2-}
P $2p_{3/2}$	130.0±0.3	1.5	Adsorbed PO_4^{3-}
P $2p_{3/2}$	131.4±0.1	1.4	Adsorbed PO_4^{3-}
P $2p_{3/2}$	132.5±0.1	1.5	Adsorbed PO_4^{3-}
P $2p_{3/2}$	133.4±0.1	1.4	$P^{(V)}$–O

[a] This peak has two multiplets located at lower and higher binding energies with 0.95 eV peak separation.

[b] This peak has three multiplets located at higher binding energies with 0.95 eV peak separation.

[c] This peak has a doublet located at a higher binding energy with 0.7 eV peak separation. The intensity ratio was constrained to two thirds with the same FWHM.

[d] This peak has a doublet located at a higher binding energy with 1.18 eV peak separation. The intensity ratio was constrained to one half with the same FWHM.

It is interesting to note that although the amount of precipitates formed by Fe-catecholate complex only was larger than that formed by Fe-catecholate complex and phosphate (Fig. 3c), the performance on arsenopyrite passivation was better when phosphate was present because dissolved As concentration stopped increasing after $FePO_4$ coating was formed (Fig. 3b). In the case when arsenopyrite was treated by Fe-catecholate complex only, dissolved As concentration was suppressed but continuously increased with time, which indicate that arsenopyrite was not fully passivated. To further evaluate the passivation effects of Fe-catecholate complex in the absence and presence of phosphate, treated arsenopyrite samples were leached again with fresh DI water (Fig. 5). As shown in Figs. 5a and 5b, the significant amounts of Fe (0.30 mM) and As (0.36 mM) were leached out from the control sample (i.e., arsenopyrite leached in DI water for 3 days); however, the releases of Fe and As decreased to 0.06 and 0.11 mM, respectively, when arsenopyrite was pretreated with Fe-catecholate complex. This indicates that Fe-catecholate complex could inhibit the oxidation of arsenopyrite via the formation of Fe-oxyhydroxide coatings

limiting the contact of water and oxidants to mineral surface. When arsenopyrite was covered with $FePO_4$ coating, the releases of Fe and As were further reduced to 0.04 and 0.09 mM, respectively. This result supports that the performance of $FePO_4$ coating in suppressing the releases of Fe and As from arsenopyrite is better than that of the coating formed by Fe-catecholate complex only. As shown in Fig. 5c, the solution pH after 1-day leaching was decreased from 6.0 to 3.8, 4.3, and 4.2 for the cases of control, Fe-catecholate complex only, and Fe-catecholate complex with phosphate, respectively, indicating that both coatings could limit arsenopyrite oxidation. However, it is important to note that the acid-resistant properties of these two coatings are different. Figure 5d shows the solubility of Fe^{3+} in the absence and presence of phosphate as a function of pH, and it implies that in the absence of phosphate, iron species becomes soluble at pH < 4 and pH > 10 while the precipitate formed in the presence of phosphate is stable in the pH range of 3–11; that is, $FePO_4$ coating would be stable in the wider pH window compared to that of Fe-oxyhydroxide coating.

Figure 6 shows the anodic polarization curves of untreated arsenopyrite electrode and the one treated with Fe-catecholate complex and phosphate. Because arsenopyrite is dissolved in the anode, changes in the anodic current densities at a certain potential could infer not only the effectiveness of coating but also the extent of dissolution of these minerals (Tabelin et al., 2017d). The anodic current density profile of treated arsenopyrite was substantially lower than that of untreated arsenopyrite. The amounts of electric charge generated/transferred during 1 h polarization of untreated and treated arsenopyrite electrodes, which were calculated based on the areas below the current density curves (Q [C] = I [A] × t [s]), were 0.5 and 0.3 mC, respectively, implying that even under strongly oxidizing conditions, the presence of $FePO_4$ coating suppressed the anodic half-cell reaction of arsenopyrite oxidation (Eq. (8)). This suppressive effect of $FePO_4$ coating on anodic dissolution of arsenopyrite is most likely achieved by (i) limiting the contact of arsenopyrite and water and/or (ii) inhibiting the diffusion of reaction products of arsenopyrite oxidation into solution.

$$FeAsS_{(s)} + 7H_2O \rightarrow Fe^{2+}{}_{(aq)} + H_3AsO_{3(aq)} + SO_4{}^{2-}{}_{(aq)} + 11H^+{}_{(aq)} + 11e^- \quad (8)$$

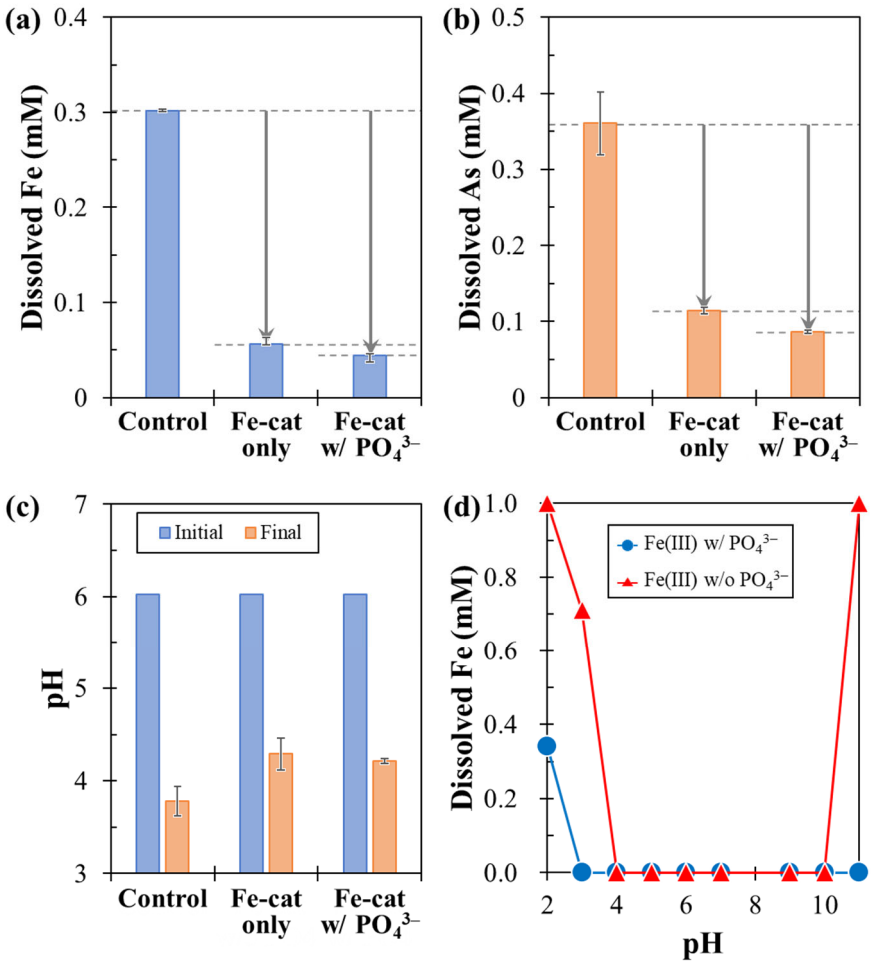

390

391 Fig. 5. Leachability tests of arsenopyrite treated in the control and by Fe-catecholate complex with and without
392 phosphate: The changes in (a) dissolved Fe concentration, (b) dissolved As concentration and (c) pH, and (d) the
393 solubility of Fe^{3+} in the absence and presence of phosphate.

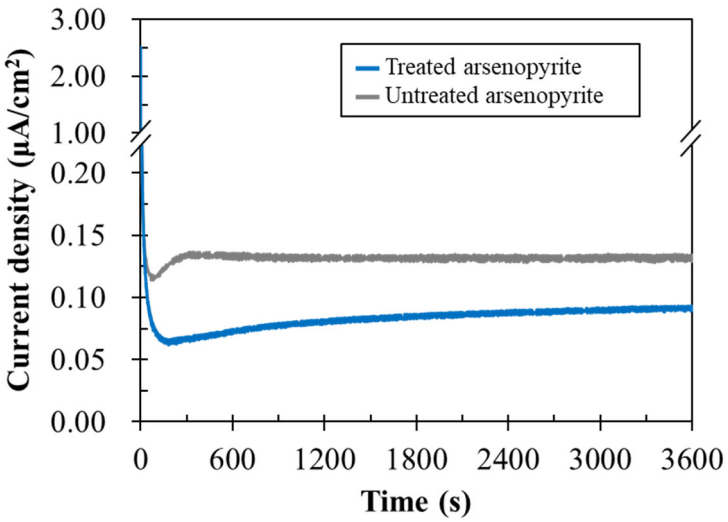

394

Fig. 6. Chronoamperometric response of untreated arsenopyrite and the one treated with Fe-catecholate complex and phosphate at an applied potential of +0.7 V vs. SHE.

4. Conclusions

Arsenopyrite oxidation plays important roles in not only releasing toxic As but also forming AMD, both of which result in serious environmental problems. This study investigated the simultaneous use of Fe-catecholate complexes and phosphate for suppressing arsenopyrite oxidation via the formation of $FePO_4$ coating on its surface. Among the three Fe-catecholate complexes, $[Fe(cat)_2]^-$ and $[Fe(cat)_3]^{3-}$ were stable regardless of the presence of phosphate while $[Fe(cat)]^+$ became unstable when phosphate coexisted. This instability of $[Fe(cat)]^+$ is highly likely caused by the replacement of catechol molecule with phosphate forming $FePO_4$. The formation of $FePO_4$ after oxidative decomposition of $[Fe(cat)_2]^-$ was evidenced by LSV. The results of SEM-EDX and XPS of arsenopyrite treated with $[Fe(cat)_2]^-$ and phosphate showed that arsenopyrite was covered with $FePO_4$ coating. Moreover, the oxidation of $FePO_4$-coated arsenopyrite was suppressed. Treatment of arsenopyrite with $[Fe(cat)_2]^-$ only also created Fe-oxyhydroxide coating and suppressed the dissolution of arsenopyrite; however, the acid-resistant property of $FePO_4$ was higher than that of Fe-oxyhydroxide under acidic conditions (pH < 4). This indicates that when treated arsenopyrite is placed in an acidic environment (pH ≈ 3), $FePO_4$ coating can survive and protect arsenopyrite from reaction with water and O_2 while Fe-oxyhydroxide would be dissolved. Thus, the use of $[Fe(cat)_2]^-$ can be an alternative way of supplying Fe^{3+} to the arsenopyrite surface in place of the use of H_2O_2 for passivating arsenopyrite with $FePO_4$ coating.

The findings of this study suggest that the passivation of arsenopyrite using $[Fe(cat)_2]^-$ and phosphate is promising for limiting the problems caused by arsenopyrite oxidation; however, its direct application to TSF would be impractical due to the acidic environment of TSF where Fe-catecholate complexes become unstable. Although this passivation technique may work in TSF by increasing its pH to neutral-alkaline conditions, it is not a sustainable approach due to the inconvenience in increasing the pH of TSF, containing acid-generating minerals and metal ions, both of which buffer against the increase in pH. In the case of sulfide ore processing, flotation is most commonly adopted as a final step to produce saleable concentrates and typically operated under neutral-alkaline conditions (pH > 7) to depress non-valuable sulfide minerals, such as pyrite and arsenopyrite (Aikawa et al., 2020; López Valdivieso et al., 2006; Park et al., 2020b). This makes the passivation technique using $[Fe(cat)_2]^-$

and phosphate applicable to flotation tailings before its disposal into TSF. After treating flotation tailings by microencapsulation using $[Fe(cat)_2]^-$ and phosphate, sulfide minerals are coated with $FePO_4$ layer, and thus the acidification of TSF as well as the release of toxic metal(loid)s caused by the oxidation of sulfide minerals are highly expected to be limited. The advantage of passivation approach is that the duration of treatment could be dramatically shortened from centuries/millennia to decades or less compared to remediation options (e.g., chemical neutralization), which makes the application of microencapsulation technique economically sound (Park et al., 2019). However, some subjects in relation to "improvement on the amount of $FePO_4$ coating" and "long-term stability of treated arsenopyrite" need to be studied further for this technique to be successfully applied to sulfide-rich mine wastes.

Acknowledgement

This study was financially supported by the Japan Society for the Promotion of Science (JSPS) grant-in-aid for scientific research (Grant number: 17H03503).

References

Ačai, P., Sorrenti, E., Gorner, T., Polakovič, M., Kongolo, M., de Donato, P., 2009. Pyrite passivation by humic acid investigated by inverse liquid chromatography. Colloids Surf., A, 337, 39–46.

Aikawa, K., Ito, M., Segawa, T., Jeon, S., Park, I., Tabelin, C.B., Hiroyoshi, N., 2020. Depression of lead-activated sphalerite by pyrite via galvanic interactions: Implications to the selective flotation of complex sulfide ores. Miner. Eng. 152, 106367.

Asamoah, R.K., Skinner, W., Addai-Mensah, J., 2018. Alkaline cyanide leaching of refractory gold flotation concentrates and biooxidised products: The effect of process variables. Hydrometallurgy 179, 79–93.

Barreiro, J.C., Capelato, M.D., Martin-Neto, L., Hansen, H.C.B., 2007. Oxidative decomposition of atrazine by a Fenton-like reaction in a H_2O_2/ferrihydrite system. Water Res. 41(1), 55–62.

Berger, B.R., Ayuso, R.A., Wynn, J.C., Seal, R.R., 2008. Preliminary model of porphyry copper deposits. USGS, Open-File Report, 1321.

449 Blowes, D.W., Jambor, J.L., Hanton-Fong, C.J., 1998. Geochemical, mineralogical and microbiological
450 characterization of a sulphide-bearing carbonate-rich gold-mine tailings impoundment, Joutel, Québec. Appl.
451 Geochem. 13(6), 687–705.

452 Boddu, V.M., Abburi, K., Talbott, J.L., Smith, E.D. Haasch, R., 2008. Removal of arsenic (III) and arsenic (V)
453 from aqueous medium using chitosan-coated biosorbent. Water Res. 42(3), 633–642.

454 Boonchom, B., Puttawong, S., 2010. Thermodynamics and kinetics of the dehydration reaction of $FePO_4 \cdot 2H_2O$.

455 Physica B 405(9), 2350–2355.

456 Bruckard, W.J., Davey, K.J., Jorgensen, F.R.A., Wright, S., Brew, D.R.M., Haque, N., Vance, E.R., 2010.
457 Development and evaluation of an early removal process for the beneficiation of arsenic-bearing copper ores.
458 Miner. Eng. 23(15), 1167–1173.

459 Chopard, A., Benzaazoua, M., Bouzahzah, H., Plante, B., Marion, P., 2017. A contribution to improve the
460 calculation of the acid generating potential of mining wastes. Chemosphere 175, 97–107.

461 Ciftci, H., Akcil, A., 2010. Effect of biooxidation conditions on cyanide consumption and gold recovery from a
462 refractory gold concentrate. Hydrometallurgy 104, 142–149.

463 Corkhill, C.L., Vaughan, D.J., 2009. Arsenopyrite oxidation – a review. Appl. Geochem. 24(12), 2342–2361.

464 Corrans, I.J., Angove, J.E., 1991. Ultra fine milling for the recovery of refractory gold. Miner. Eng. 4, 763–776.

465 Deol, S., Deb, M., Large, R.R., Gilbert, S., 2012. LA-ICPMS and EPMA studies of pyrite, arsenopyrite and
466 loellingite from the Bhukia-Jagpura gold prospect, southern Rajasthan, India: Implications for ore genesis and
467 gold remobilization. Chem. Geol. 326–327, 72–87.

468 Dong, Y., Zeng, W., Lin, H., and He, Y., 2020. Preparation of a novel water-soluble organosilane coating and its
469 performance for inhibition of pyrite oxidation to control acid mine drainage at the source. Appl. Surf. Sci. 531,
470 147328.

471 Dunn, J.G., Chamberlain, A.C., 1997. The recovery of gold from refractory arsenopyrite concentrates by
472 pyrolysis-oxidation. Miner. Eng. 10(9), 919–928.

473 Elsetinow, A.R., Schoonen, M.A., Strongin, D.R., 2001. Aqueous geochemical and surface science investigation

474 of the effect of phosphate on pyrite oxidation. Environ. Sci. Technol. 35(11), 2252-2257.

475 Elsetinow, A.R., Borda, M.J., Schoonen, M.A.A., Strongin, D.R., 2003. Suppression of pyrite oxidation in acidic
476 aqueous environments using lipids having two hydrophobic tails. Adv. Environ. Res., 7, 969–974.

477 Evangelou, V.P., 1995. Pyrite Oxidation and its Control. CRC press, Boca Raton, FL.

478 Fan, L., Zhao, F., Liu, J., Hudson-Edwards, K.A., 2018. Dissolution of realgar by *Acidithiobacillus ferrooxidans*
479 in the presence and absence of zerovalent iron: Implications for remediation of iron-deficient realgar tailings.
480 Chemosphere 209, 381–391.

481 Gudyanga, F.P., Mahlangu, T., Roman, R.J., Mungoshi, J., Mbeve, K., 1999. An acidic pressure oxidation
482 pretreatment of refractory gold concentrates from the KweKwe roasting plant, Zimbabwe. Miner. Eng. 12(8),
483 863–875.

484 Grosvenor, A. P., Kobe, B. A., Biesinger, M. C., McIntyre, N. S., 2004. Investigation of multiplet splitting of Fe
485 2p XPS spectra and bonding in iron compounds. Surf. Interface Analy. 36, 1564–1574.

486 Han, Y.-S., Jeong, H.Y., Demond, A.H., Hayes, K.F., 2011. X-ray absorption and photoelectron spectroscopic
487 study of the association of As(III) with nanoparticulate FeS and FeS-coated sand. Water res. 45(17), 5727–5735.

488 Huyen, D.T., Tabelin, C.B., Thuan, H.M., Dang, D.H., Truong, P.T., Vongphuthone, B., Kobayashi, M., Igarashi,
489 T., 2019a. The solid-phase partitioning of arsenic in unconsolidated sediments of the Mekong Delta, Vietnam and
490 its modes of release under various conditions. Chemosphere 233, 512–523.

491 Huyen, D.T., Tabelin, C.B., Thuan, H.M., Danga, D.H., Truong, P.T., Vongphuthone, B., Kobayashi, M., Igarashi,
492 T., 2019b. Geological and Geochemical Characterizations of Sediments in Six Borehole Cores from the Arsenic-
493 Contaminated Aquifer of the Mekong Delta. Vietnam. Data in Brief, 104230.

494 Igarashi, T., Herrera, S.P., Uchiyama, H., Miyamae, H., Iyatomi, N., Hashimoto, K., Tabelin, C.B., 2020. The two-
495 step neutralization ferrite-formation process for sustainable acid mine drainage treatment: removal of copper, zinc
496 and arsenic, and the influence of coexisting ions on ferritization. Sci. Total Environ. 715, 136877.Jiang, C.L.,
497 Wang, X.H., Parekh, B.K., 2000. Effect of sodium oleate on inhibiting pyrite oxidation. Int. J. Miner. Process., 58,
498 305–318.

499 John, D.A., Ayuso, R.A., Barton, M.D., Blakely, R.J., Bodnar, R.J., Dilles, J.H., Gray, F., Graybeal, F.T., Mars,

J.C., McPhee, D.K., Seal, R.R., Taylor, R.D., Vikre, P.G., 2010. Porphyry copper deposit model, Chapter B of Mineral deposit models for resource assessment: U.S. Geological Survey Scientific Investigations Report 2010–5070–B, 169 p.

John, D.A., Taylor, R.D., 2016. By-products of porphyry copper and molybdenum deposits. Rev. Econ. Geol. 18, 137–164.

Lane, D.J., Cook, N.J., Grano, S.R., Ehrig, K., 2016. Selective leaching of penalty elements from copper concentrates: A review. Miner. Eng. 98, 110–121.

Lara, R.H., Velázquez, L.J., Vazquez-Arenas, J., Mallet, M., Dossot, M., Labastida, I., Sosa-Rodríguez, F.S., Espinosa-Cristóbal, L.F., Escobedo-Bretado, M.A. Cruz, R., 2016. Arsenopyrite weathering under conditions of simulated calcareous soil. Environ. Sci. Pollut. Res., 23, 3681–3706.

Li, X., Hiroyoshi, N., Tabelin, C.B., Naruwa, K., Harada, C., Ito, M., 2019. Suppressive effects of ferric-catecholate complexes on pyrite oxidation. Chemosphere 214, 70-78.

Liu, X., Li, Q., Zhang, Y., Jiang, T., Yang, Y., Xu, B., He, Y., 2020. Electrochemical behavior of the dissolution and passivation of arsenopyrite in 9K culture medium. Appl. Surf. Sci. 508, 145269.

Liu, Y., Hu, X., and Xu, Y., 2017. PropS-SH/SiO_2 nanocomposite coatings for pyrite oxidation inhibition to control acid mine drainage at the source. J. Hazard. Mater. 338, 313–322.

López Valdivieso, A., Sánchez López, A.A., Ojeda Escamilla, C., Fuerstenau, M.C., 2006. Flotation and depression control of arsenopyrite through pH and pulp redox potential using xanthate as the collector. Int. J. Miner. Proc. 81(1), 27–34.

McKibben, M.A., Tallant, B.A., del Angel, J.K., 2008. Kinetics of inorganic arsenopyrite oxidation in acidic aqueous solutions. Appl. Geochem. 23, 121–135.

Mesa Espitia, S.L., Lapidus, G.T., 2015. Pretreatment of a refractory arsenopyritic gold ore using hydroxyl ion. Hydrometallurgy 153, 106–113.

Mohan, D., Pittman Jr., C.U., 2007. Arsenic removal from water/wastewater using adsorbents – a critical review. J. Hazard. Mater. 142(1–2), 1–53.

Nazari, A.M., Radzinski, R., Ghahreman, A., 2017. Review of arsenic metallurgy: Treatment of arsenical minerals

526 and the immobilization of arsenic. Hydrometallurgy 174, 258–281.

527 Nesbitt, H.W., Muir, I.J., 1994. X-ray photoelectron spectroscopic study of a pristine pyrite surface reacted with
528 water vapour and air. Geochem. Cosmochim. Acta, 58, 4667–4679.

529 Nesbitt, H.W., Muir, I.J., Pratt, A.R., 1995. Oxidation of arsenopyrite by air and air-saturated, distilled water, and
530 implications for mechanism of oxidation. Geochem. Cosmochim. Acta, 59(9), 1773–1786.

531 Ouyang, Y., Liu, Y., Zhu, R., Ge, F., Xu, T., Luo, Z., Liang, L., 2015. Pyrite oxidation inhibition by organosilane
532 coatings for acid mine drainage control. Miner. Eng. 72, 57–64.

533 Park, I., Tabelin, C.B., Magaribuchi, K., Seno, K., Ito, M., Hiroyoshi, N., 2018a. Suppression of the release of
534 arsenic from arsenopyrite by carrier-microencapsulation using Ti-catechol complex. J. Hazard. Mater. 344, 322–
535 332.

536 Park, I., Tabelin, C.B., Seno, K., Jeon, S., Ito, M., Hiroyoshi, N., 2018b. Simultaneous suppression of acid mine
537 drainage formation and arsenic release by Carrier-microencapsulation using aluminum-catecholate complexes.
538 Chemosphere 205, 414–425.

539 Park, I., Tabelin, C.B., Jeon, S., Li, X., Seno, K., Ito, M., Hiroyoshi, N., 2019. A review of recent strategies for
540 acid mine drainage prevention and mine tailings recycling. Chemosphere 219, 588–606.

541 Park, I., Tabelin, C.B., Seno, K., Jeon, S., Inano, H., Ito, M., Hiroyoshi, N., 2020a. Carrier-microencapsulation of
542 arsenopyrite using Al-catecholate complex: nature of oxidation products, effects on anodic and cathodic reactions,
543 and coating stability under simulated weathering conditions. Heliyon 6(1), e03189.

544 Park, I., Hong, S., Jeon, S., Ito, M., Hiroyoshi, N., 2020b. A review of recent advances in depression techniques
545 for flotation separation of Cu–Mo sulfides in porphyry copper deposits. Metals 10(9), 1269.

546 Pokrovski, G.S., Kokh, M.A., Proux, O., Hazemann, J.-L., Bazarkina, E.F., Testemale, D., Escoda, C., Boiron,
547 M.-C., Blanchard, M., Aigouy, T., Gouy, S., de Parseval, P., Thibaut, M., 2019. The nature and partitioning of
548 invisible gold in the pyrite-fluid system. Ore Geol. Rev. 109, 545–563.

549 Praneetha, S., Murugan, A.V., 2013. A rapid, one-pot microwave-solvothermal synthesis of a hierarchical
550 nanostructured graphene/$LiFePO_4$ hybrid as a high performance cathode for lithium ion batteries. RSC Adv. 3,
551 25403–25409.

552 Shirley, D.A., 1972. High-resolution X-ray photoemission spectrum of the valence bands of gold. Phys. Rev. B,
553 5, 4709–4714.

554 Tabelin, C.B., Igarashi, T., 2009. Mechanisms of arsenic and lead release from hydrothermally altered rock. J.
555 Hazard Mater. 169, 980–990.

556 Tabelin, C.B., Igarashi, T., Yoneda, T., Tamamura, S., 2013. Utilization of natural and artificial adsorbents in the
557 mitigation of arsenic leached from hydrothermally altered rock. Eng. Geol. 156, 58–67.

558 Tabelin, C.B., Sasaki, R., Igarashi, T., Park, I., Tamoto, S., Arima, T., Ito, M., Hiroyoshi, N., 2017a. Simultaneous
559 leaching of arsenite, arsenate, selenite, and selenate, and their migration in tunnel-excavated sedimentary rocks:
560 I. Column experiments under intermittent and unsaturated flow. Chemosphere 186, 558–569.

561 Tabelin, C.B., Sasaki, R., Igarashi, T., Park, I., Tamoto, S., Arima, T., Ito, M., Hiroyoshi, N., 2017b. Simultaneous
562 leaching of arsenite, arsenate, selenite, and selenate, and their migration in tunnel-excavated sedimentary rocks:
563 II. Kinetic and reactive transport modeling. Chemosphere 188, 444–454.

564 Tabelin, C.B., Veerawattananun, S., Ito, M., Hiroyoshi, N. and Igarashi, T., 2017c. Pyrite oxidation in the presence
565 of hematite and alumina: I. Batch leaching experiments and kinetic modeling calculations. Sci. Total Environ. 580,
566 687–698.

567 Tabelin, C.B., Veerawattananun, S., Ito, M., Hiroyoshi, N., Igarashi, T., 2017d. Pyrite oxidation in the presence of
568 hematite and alumina: II. Effects on the cathodic and anodic half-cell reactions. Sci. Total Environ. 581–582, 126–
569 135.

570 Tabelin, C.B., Igarashi, T., Villacorte-Tabelin, M., Park, I., Opiso, E.M., Ito, M., Hiroyoshi, N., 2018. Arsenic,
571 selenium, boron, lead, cadmium, copper, and zinc in naturally contaminated rocks: a review of their sources,
572 modes of enrichment, mechanisms of release, and mitigation strategies. Sci. Total Environ. 645, 1522–1553.

573 Tabelin, C.B., Silwamba, M., Paglinawan, F.C., Mondejar, A.J.S., Duc, H.G., Resabal, V.J., Opiso, E.M., Igarashi,
574 T., Tomiyama, S., Ito, M. and Hiroyoshi, N., 2020a. Solid-phase partitioning and release-retention mechanisms of
575 copper, lead, zinc and arsenic in soils impacted by artisanal and small-scale gold mining (ASGM) activities.
576 Chemosphere, 127574.

577 Tabelin, C.B., Corpuz, R.D., Igarashi, T., Villacorte-Tabelin, M., Alorro, R.D., Yoo, K., Raval, S., Ito, M.,

578 Hiroyoshi, N., 2020b. Acid mine drainage formation and arsenic mobility under strongly acidic conditions:
579 importance of soluble phases, iron oxyhydroxides/oxides and nature of oxidation layer on pyrite. J. Hazard. Mater.
580 399, 122844.

581 Tatsuhara, T., Arima, T., Igarashi, T., Tabelin, C.B., 2012. Combined Neutralization-adsorption system for the
582 disposal of hydrothermally altered excavated rock producing acidic leachate with hazardous elements. Eng. Geol.
583 139, 76–84.

584 Tomiyama, S., Igarashi, T., Tabelin, C.B., Tangviroon, P., Ii, H., 2019. Acid mine drainage sources and
585 hydrogeochemistry at the Yatani mine, Yamagata, Japan: a geochemical and isotopic study. J. Contam. Hydrol.
586 225, 103502.

587 Tomiyama, S., Igarashi, T., Tabelin, C.B., Tangviroon, P., Ii, H., 2020. Modeling of the groundwater flow system
588 in excavated areas of an abandoned mine. J. Contam. Hydrol. 230, 103617.USEPA, 2001. National primary
589 drinking water regulations: arsenic and clarifications to compliance and new source contaminants monitoring.
590 Federal Register 66(14), 69–76.

591 Wang, Z., Liu, E., He, C., Shi, C., Li, J., Zhao, N., 2013. Effect of amorphous $FePO_4$ coating on structure and
592 electrochemical performance of $Li_{1.2}Ni_{0.13}Co_{0.13}Mn_{0.54}O_2$ as cathode material for Li-ion batteries. J. Power Sources
593 236, 25–32.

594 Yamaguchi, K., Tomiyama, S., Metugi, H., Ii, H., Ueda, A., 2015. Flow and geochemical modeling of drainage
595 from Tomitaka mine, Miyazaki, Japan. J. Environ. Sci. 36, 130–143.

596 Zaghib, K., Julien, C.M., 2005. Structure and electrochemistry of $FePO_4 \cdot 2H_2O$ hydrate. J. Power Sources 142,
597 279–284.

598 Zeng, L., Li, X., Shi, Y., Qi, Y., Huang, D., Tadé, M., Wang, S., Liu, S., 2017. $FePO_4$ based single chamber air-
599 cathode microbial fuel cell for online monitoring levofloxacin. Biosens. Bioelectron. 91, 367–373.

600 Zhou, J., Shan, X., Ma, J., Gu, Y., Qian, Z., Chen, J., Feng, H., 2014. Facile synthesis of P-doped carbon quantum
601 dots with highly efficient photoluminescence. RSC Adv. 4, 5465–5468.

602 Zhu, T., Lu, X., Liu, H., Li, J., Zhu, X., Lu, J., Wang, R., 2014. Quantitative X-ray photoelectron spectroscopy-
603 based depth profiling of bioleached arsenopyrite surface by Acidithiobacillus ferrooxidans. Geochem. Cosmochim.

Acta, 127, 120–139.